RSC Advances



PAPER

View Article Online
View Journal | View Issue



Cite this: RSC Adv., 2020, 10, 2581

Self-assembled CeVO₄/Au heterojunction nanocrystals for photothermal/photoacoustic bimodal imaging-guided phototherapy†

Junrong Wang, ^a Yubo Hu, ^b Junyang Chen^b and Cong Ye ^{(b)*a}

Phototherapy, including photothermal therapy (PTT) and photodynamic therapy (PDT), has attracted great attention because it can effectively inhibit the proliferation and propagation of cancer cells. Recently, heterojunction nanomaterials have shown tremendous application value in the field of biological medicine. In this work, the CeVO₄/Au heterojunction nanocrystals (NCs) are designed for photothermal/photoacoustic bimodal imaging-guided phototherapy. The as-synthesized hydrophobic oleic acid (OA)-stabilized CeVO₄ nanosheets were modified with HS-PEG-OH for translating into hydrophilic ones, which can significantly improve their stability and biocompatibility. Subsequently, the plasmonic Au nanoparticles were *in situ* successfully deposited on the surface of HS-PEG-coated CeVO₄ to form CeVO₄/Au heterojunction NCs for improving the visible and near-infrared light absorption, which results in enhanced photothermal conversion performance and reactive oxygen species (ROS) generation capacity. Thus, the CeVO₄/Au can cause more severe damage to cancer cells than pure CeVO₄ under NIR laser irradiation. Also, CeVO₄/Au can provide distinct tumor contrast by photothermal/photoacoustic bimodal bioimaging. Our results demonstrate that CeVO₄/Au NCs could be used as an effective theranostic anticancer agent for near-infrared (NIR) light-mediated PTT and PDT.

Received 25th November 2019 Accepted 4th January 2020

DOI: 10.1039/c9ra09860g

rsc.li/rsc-advances

Introduction

Cancer has a very serious impact on human health, which causes high mortality worldwide.1-5 Although surgery,6 chemotherapy⁷⁻⁹ and radiotherapy^{10,11} are considered to be the main treatment approaches for cancer, they have many disadvantages, such as surgical risks and complications, serious side effects and the metastasis of residual cancer cells. Phototherapy, including photothermal and photodynamic therapy, was identified as an emerging noninvasive treatment method and has become a powerful candidate to replace traditional therapeutic methods because it can effectively inhibit the proliferation and propagation of cancer cells. 12-14 Photothermal therapy (PTT) can effectively kill target cancer cells by utilizing NIR laser irradiation to produce heat energy from light energy.15-17 In recent years, a series of photothermal agents, including gold nanoparticles (NPs),18-20 carbon-based nanosheets,21 metal chalcogenides,22-25 and conjugated polymers26,27

Inorganic semiconductor nanomaterials have been widely used as photothermal agents,³⁸ photosensitizes³⁹ and multimode imaging agents⁴⁰⁻⁴² due to their unique optical performance. Cerium vanadate (CeVO₄), a kind of wide band gap inorganic semiconductor nanomaterials,⁴³ has relatively small optical cross-sections in the Vis/NIR regions.⁴⁴ Thus, it was rarely applied as NIR-responsive anticancer agents.⁴⁵ The local surface plasmon resonance (LSPR)⁴⁶ offers a new strategy to enhance the optical absorption of semiconductor nanomaterials through loading plasmonic metal nanoparticles (NPs)

have been used in PTT. Photodynamic therapy (PDT) can transfer the absorbed light to produce toxic reactive oxygen species (ROS) under NIR laser irradiation by exciting the photosensitizer molecules, in particular oxidative species ($\cdot O_2^-$) can cause significant cancer cell apoptosis and necrosis. 13,28,29 Recently, the semiconductor NPs (such as TiO2, 30 ZnO, 31 Fe3-O4@SiO2-CdTe32), metal phthalocyanines,33 and chlorin derivatives³⁴ have been used as photosensitizers for PDT by exciting the electron-hole pairs separation. In addition, the imaging technology such as photothermal (PT) imaging and photoacoustic (PA) imaging has been introduced for accurate diagnosis and treatment of cancer. The PT imaging can directly show the therapeutic effect of PTT through monitoring macroscopic temperature change. And the (PA) imaging provides a promising biomedical imaging modality, which provides higher spatial resolution and relatively deeper tissue penetration through the detection of ultrasonic signal waves.35-37

^aDepartment of Obstetrics and Gynecology, China-Japan Union Hospital of Jilin University, Changchun, Jilin 130033, China. E-mail: zhanggs576@163.com

^bDepartment of Anesthesiology, China-Japan Union Hospital of Jilin University, Changchun, Jilin 130033, China

[†] Electronic supplementary information (ESI) available: Experimental section, zeta potential, hydrodynamic size, photothermal activity, DPBF depletion, MB depletion, linear relationship between PA signal and sample concentration, blood panel and serum biochemical index parameters. See DOI: 10.1039/c9ra09860g

on the surface of semiconductor NCs. $^{47-51}$ Integrating plasmonic Au NPs with various semiconductors nanomaterials to form heterojunction nanostructures, such as Au@SiO₂@Cu₂O, 52 Bi₂S₃@Au, 53 Au@CuS, 54 CuS@Cu₂S@Au, 55 Au/TiO₂, 56 Au@PB@Cu₂O@ BPQDs/PAH, 57 Au@NdVO₄, 49 Au/Fe₃O₄, 58 could significantly expand the light absorption range to improve the photo-conversion performance.

Herein, we have successfully obtained CeVO₄/Au heterojunction NCs in this study (Scheme 1). Firstly, the oleic acid (OA)stabilized CeVO₄ nanosheets were prepared through hydrothermal method.⁵⁹ Next, the (OA)-stabilized CeVO₄ was modified by HS-PEG-OH through thiolene click reaction. These modified materials can improved biocompatibility and stability.32,60-64 Finally, Au NPs were in situ successfully deposited on the surface of HS-PEG-coated CeVO₄ to form CeVO₄/Au heterojunction NCs. Once CeVO₄/Au was transferred into water from THF, they presented self-assembled morphology due to hydrophobic-hydrophobic interactions because the OA-coated CeVO₄ didn't completely modified by HS-PEG-OH. Due to the LSPR effect of Au, the CeVO₄/Au NCs represents enhanced separation efficiency of electron and hole pairs and increased optical absorption in Vis/ NIR region, resulting in improved ROS generation capability and photothermal conversion performance. Therefore, the CeVO₄/Au could cause severe damage to cancer cells than CeVO₄ under NIR laser irradiation. Also, the CeVO₄/Au can provide distinct tumor contrast by photothermal/photoacoustic bimodal bioimaging. Our results demonstrate that CeVO₄/Au NCs could be used as an effective theranostic anticancer agent for nearinfrared (NIR) light-mediated PTT and PDT.

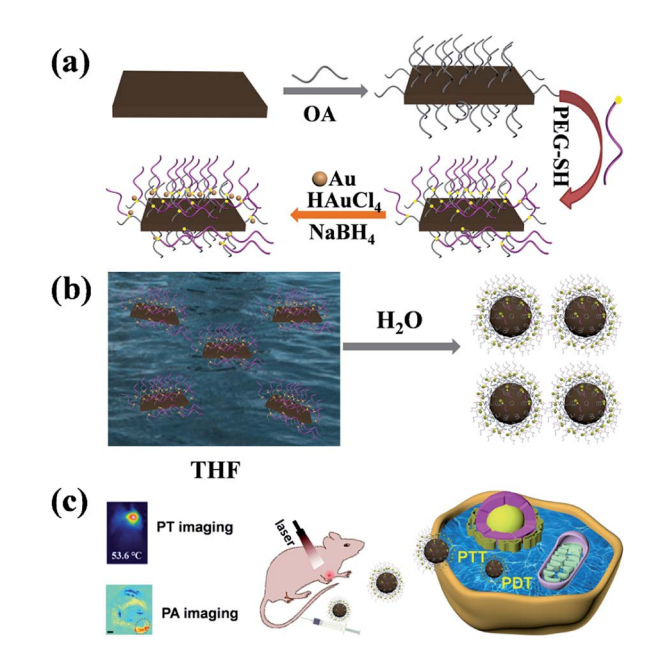
Experimental section

Synthesis of oleic acid-capped CeVO₄ nanosheets

NaOH (0.6 g) and NH₄VO₃ (0.0585 g) were added into 5 mL of deionized water under magnetic stir. A mixed solution of oleic acid (9 mL) and ethanol (10 mL) was added into the above solution. Then, 1 mL of Ce(NO₃)₃·6H₂O aqueous solution (1 M) was added dropwise. After stirring for 10 min, the mixed solution was sealed in a 40 mL Teflon-lined autoclave (140 °C, 8 h), then slowly cooled to room temperature, the samples were collected and dissolved in cyclohexane. Finally, CeVO₄ nanosheets were isolated by centrifugation at 3000 rpm (5 min), and washed with cyclohexane and ethanol. Afterward, the CeVO₄ nanosheets were distributed in 5 mL cyclohexane.

Synthesis of HS-PEG-functionalized CeVO₄ nanosheets

The 2 mL of above CeVO $_4$ nanosheets were precipitated by adding enough ethanol and isolated by centrifugation at 3000 rpm for 5 min. Then the samples were dissolved into 2 mL of THF solution. Then 0.2 g of HS-PEG-OH and 100 μ L of photoinitiator DMPA (10 mg mL $^{-1}$) dissolved in THF were added. The mixture was irradiated with UV-light (1000 W, 365 nm wavelength) for 60 min in an ice bath under stirring. After completion of UV irradiation, the HS-PEG-functionalized CeVO $_4$ nanosheets were isolated by centrifugation at 12 000 rpm (15 min), and washed with water.



Scheme 1 Schematic illustration of the synthesis process (a), self-assembly process (b) and biological application (c) of $CeVO_4/Au$.

Synthesis of CeVO₄/Au heterojunction NCs

The above HS-PEG functionalized CeVO $_4$ nanosheet was distributed in ethanol (1.2 mL). After stirring for 30 min, 100 μ L of HAuCl $_4$ ·3H $_2$ O aqueous solution (0.029 M) was added. After stirring for 10 min, 50 μ L of NaBH $_4$ (0.06 M) was added and stirred for 30 min. The CeVO $_4$ /Au NCs were centrifuged at 12 000 rpm (10 min), and washed with ethanol. Afterward, the products were distributed in deionized water.

Toxicology evaluation

The CeVO₄/Au (20 mg kg $^{-1}$, 100 μ L) was tail vein injected into healthy Blab/c mice and the mice injected with normal saline as a control group. For the blood of the experimental group and control group was collected (1 day, 7 days and 14 days postinjection). And then the blood panel and serum biochemical analysis were carried on.

Bio-distribution of CeVO₄/Au in mice

The CeVO₄/Au (20 mg kg⁻¹, 100 μ L) was tail vein injected into U14 tumor-bearing Balb/c mice. Then the mice (N=4) were euthanized at different time points (1 hour, 4 hours, 8 hours, 12 hours, 1 day, 3 days and 7 days). The major organs (heart, liver, spleen, lung, and kidney) and tumor were collected and weighed. Afterward, these organs were dealt with concentrated nitric acid and H_2O_2 [V (HNO₃) : V (H_2O_2) = 1 : 2] on heating (70 °C) until they became clear. The concentrations of Ce and Au were detected by inductively coupled plasma mass spectrometry (ICP-MS), and were calculated in each organ and tumor.

Paper

Live-dead cell staining experiments

HeLa cells were seeded at a density of 0.2×10^5 cells per well in 24-well culture plates and incubated at 37 °C in 5% CO₂ for 24 h. Afterward, HeLa cells were incubated with 400 μL of CeVO₄ or CeVO₄/Au (200 $\mu g \text{ mL}^{-1}$) at 37 °C for 4 hours. Then, the culture media were replaced with fresh medium, and exposed to NIR laser irradiation (1.0 W cm⁻²) for 5 min. After that, the live cells were stained with Calcein-AM (green fluorescence) and the dead cells were stained with pyridine iodide (PI) (red fluorescence).

Histological analysis

For hematoxylin and eosin (H&E) staining, major organs (heart, liver, spleen, lung, and kidney) and tumor were harvested, fixed in 10% neutral buffered formalin, processed routinely into paraffin, sectioned into thin slices and stained with H&E for histological analysis at day 14.

Photothermal (PT) imaging

For in vitro PT imaging, the CeVO₄ solution and CeVO₄/Au solution (200 µg mL⁻¹, 100 µL) were exposed to a cuvette and were placed on NIR laser irradiation (1.0 W cm⁻²) for 5 min. The real-time temperature was detected and recorded by an infrared camera. For in vivo PT imaging, U14 cells were subcutaneously inoculated into the left armpit of Blab/c mice. While the tumor volume changes reached about 100 mm³, normal saline (100 μL), CeVO₄ and CeVO₄/Au (20 mg kg⁻¹) were tail vein injected, respectively. After 8 h post-injection, the tumor was exposed to NIR laser irradiation (0.5 W cm⁻²), and PT images were captured by an infrared camera.

Photoacoustic (PA) imaging

To measure the photoacoustic (PA) signal sensitivity of CeVO₄ and CeVO₄/Au, a phantom filled with the different concentrations of NCs (10, 20, 40, 80 and 160 μ g mL⁻¹) was measured using a real-time multispectral optoacoustic tomographic (MSOT) imaging system (inVision 128, iThera Medical GmbH, Neuherberg, Germany). Subsequently, the phantom was placed into a water tank and imaged at the 680-980 nm laser. Finally, the PA signals were measured in regions of interest (ROIs) for each sample and the correlation between the PA signal and concentration response curve was calculated.

To perform in vivo PA imaging, CeVO₄ and CeVO₄/Au NCs (20 mg kg⁻¹, 100 μL) were tail vein injected into the tumorbearing mice. After 8 h, the mice were placed in a container surrounded by a polyethylene film. In all data acquisitions, the light fibers and ultrasonic sensor arrays were in a fixed position. The mice were scanned before and after tail vein injection. ROIs were chosen and the PA signal was analyzed using ViewMOSTTM software.

Animal xenograft model

Female Balb/c mice (six weeks old) were purchased from the Center for Experimental Animals, Jilin University. All animal studies were conducted in accordance with the guidelines of the National Regulation of China for Care and Use of Laboratory

Animals. The U14 tumor models were successfully established by subcutaneous injection of 4×10^6 cells suspended in 100 μ L PBS into the left armpit of each mouse. The mice were treated when the tumor volumes approached 100 mm³.

Results and discussion

Preparation and characterization of the CeVO₄ and CeVO₄/Au

The preparation process of CeVO₄/Au was showed in Scheme 1. Firstly, the oleic acid (OA)-stabilized CeVO4 nanosheets were prepared through the hydrothermal method,59 which exhibits square-like sheet morphology as shown in the transmission electron microscopy (TEM) image (Fig. 1A). And the characteristic diffraction peaks of CeVO4 in powder X-ray diffraction (XRD) patterns match well with those of the tetragonal phase (CeVO₄, JCPDS 82-1969) (Fig. 1B). Afterward, the (OA)-stabilized CeVO₄ surface was modified by the HS-PEG-OH⁶⁰ for transforming hydrophobic CeVO4 into hydrophilic and enhancing biocompatibility. On the basis of the FT-IR spectroscopy (Fig. 1C), we concluded that the =C-H stretching vibration appears at 3006 cm⁻¹ decreased and the stretching vibration owing to -CH₂-O- at 1106 cm⁻¹ is gradually enhanced, which demonstrate that the OA-stabilized CeVO4 was successfully modified by HS-PEG-OH. Finally, Au nanoparticles were in situ deposited on the surface of HS-PEG-coated CeVO4 via the reduction of HAuCl₄ by NaBH₄. Fig. 1D shows the TEM image of as-prepared CeVO₄/Au heterojunction nanocrystals, which presents self-assembled morphology due to hydrophobichydrophobic interactions because the OA-coated CeVO4 didn't completely modified by HS-PEG-OH. According to the highresolution transmission electron microscopy (HR-TEM) image (Fig. 1E), the lattice fringes of CeVO₄/Au nanohybrids display interplanar spacings of 0.2355 nm and 0.2949 nm, which match well with those of the (111) and the (211) planes of Au and CeVO₄, respectively. As can be seen from the elemental mapping (Fig. 1F), the elements of Ce, V, O, C, S and Au are

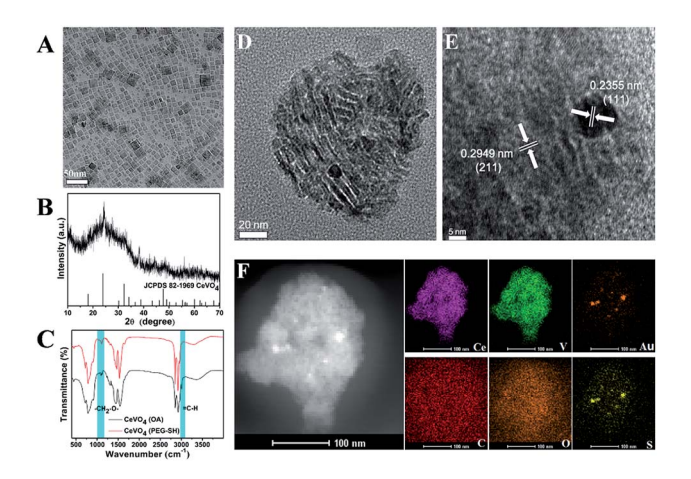


Fig. 1 (A) TEM images of the OA-capped CeVO₄ dispersed in hexane; (B) XRD patterns of OA-capped CeVO₄; (C) FTIR spectra of OA-capped CeVO₄ and CeVO4 modified by HS-PEG-OH; (D) TEM image of CeVO₄/Au; (E) HR-TEM image and (F) EDS elemental mapping of CeVO₄/Au.

presented in the CeVO $_4$ /Au nanohybrids. And the changed zeta potential from 20.3 to -6.3 mV further verified the formation of CeVO $_4$ /Au (Fig. S1 †). Moreover, the average hydrodynamic particle sizes of CeVO $_4$ /Au is about 127.5 nm, which could maintain constant within seven days in various physiological solutions (Fig. S2 †).

Photothermal properties contrast among CeVO₄ and CeVO₄/Au

The CeVO₄/Au displays exceptional optical properties due to LSPR of Au NPs as compared to pure CeVO₄. According to the UV-Vis-NIR spectroscopy (Fig. 2A), a slight blue-shift of the Ce³⁺ characteristic absorption from 285 to 275 nm was observed due to the formation of CeVO₄/Au nanohybrids. More importantly, the obviously enhanced absorption of CeVO₄/Au could be found in the Vis/NIR region, which stimulated our study of the photothermal properties of CeVO₄/Au. The temperature elevation of CeVO₄, CeVO₄/Au, and water under NIR (1.0 W cm⁻²) laser irradiation was showed in Fig. 2B. The temperature of CeVO₄/Au aqueous solution increased to 54.7 °C, while that of CeVO₄ solution and water only increase to 40 °C and 28.9 °C, respectively. In addition, both CeVO₄/Au and CeVO₄ showed concentration and power density-dependent temperature evolution activity (Fig. S3A-D†). However, the CeVO₄/Au solution displayed a more excellent photothermal conversion performance than pure CeVO₄ solution. According to the obtained test result (Fig. 2C and S4†), the time constant (τ_s) for the cooling process of CeVO₄/Au and CeVO₄ are determined to be 488.63 s and 581.51 s, respectively. Meanwhile, the photothermal conversion efficiency (η) of CeVO₄/Au and CeVO₄ were calculated to be 17.32% and 11.65%, respectively. Moreover, the photothermal conversion performance of CeVO₄/Au is almost no change after

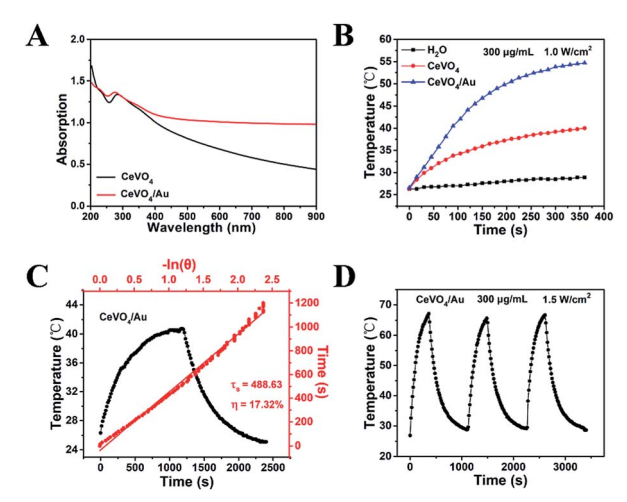


Fig. 2 (A) Vis/NIR absorption spectra of CeVO₄ and CeVO₄/Au. (B) Photothermal activity of CeVO₄ and CeVO₄/Au (300 μg mL $^{-1}$) under 1.0 W cm $^{-2}$ of NIR laser irradiation for 5 min. (C) The temperature change of CeVO₄/Au aqueous solution (300 μg mL $^{-1}$, 1 mL) response to 1.3 W cm $^{-2}$ of NIR laser on and off and Linear time data versus—ln θ obtained from the cooling period of CeVO₄/Au aqueous solution. (D) The PT conversion cycling test of CeVO₄/Au aqueous solution under 1.0 W cm $^{-2}$ of NIR laser irradiation.

three cycles of heating and cooling (heating 6 min and cooling 12 min for one cycle, Fig. 2D). Collectively, these results validate that CeVO₄/Au heterojunction NCs are more excellent photothermal conversion agent than pure CeVO₄ due to the LSPR of Au NPs.

The ROS detection

The production capability of reactive oxygen species (ROS) over CeVO₄ and CeVO₄/Au heterojunction NCs upon NIR laser irradiation was further studied. As a result of LSPR excitation, Au NPs could generate hot electrons through absorbing resonant photons and transmit them to the adjacent CeVO₄, which surmounts the wide band gap of CeVO4 and leads to effective separation of electrons-holes pairs in CeVO₄/Au heterojunction NCs. In the first place, Au NPs could produce hot electrons upon resonant excitation. These hot electrons could focus on the conduction band (CB) of the CeVO₄ by hot-electrons injection process,65,66 and they could be seized by molecular oxygen (O2) to produce ·O₂⁻. The 1,3-diphenylisobenzofuran (DPBF) probe was used to monitor the performance of CeVO4 and CeVO4/Au to generate $\cdot O_2^-$ under photo-excitation. On the basis of Fig. 3A and S5,† we concluded that the absorption intensity of DPBF decreased distinctly with the increasing of NIR laser irradiation time in the CeVO₄/Au group, while that of the CeVO₄ group was almost unchanged. In order to eliminate the interference of oxygen, we detected the fluorescence intensity of singlet oxygen sensor green (SOSG, highly specific fluorescent indicator to ${}^{1}O_{2}$) in the presence of CeVO4 and CeVO4/Au with NIR laser (1.0 W cm⁻²) irradiation. As displayed in Fig. S6,† we concluded that the fluorescence intensity of SOSG were almost unchanged with the increasing of NIR laser irradiation time in the CeVO₄/Au group and the CeVO₄ group. From the results we have obtained

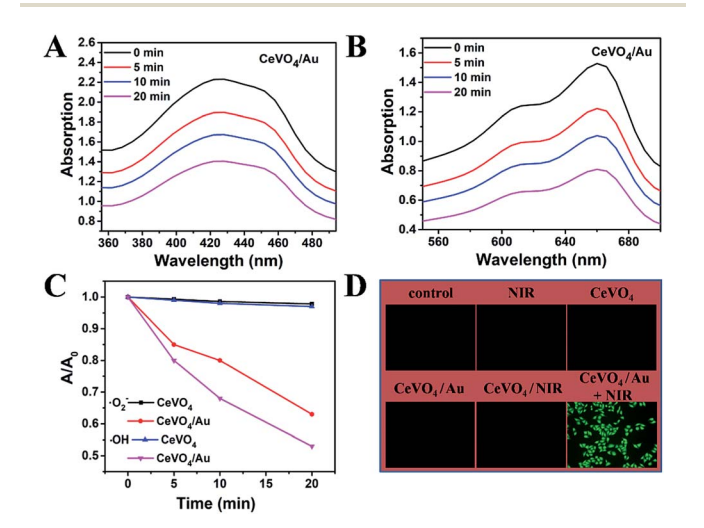


Fig. 3 (A) Depletion of DPBF due to \cdot O $_2$ ⁻ generation: 65 μg mL $^{-1}$ of CeVO $_4$ /Au with NIR laser (1.0 W cm $^{-2}$) irradiation. (B) Depletion of MB due to \cdot OH generation: 65 μg mL $^{-1}$ of NdVO $_4$ /Au with NIR laser (1.0 W cm $^{-2}$) irradiation. (C) The comparison of \cdot OH and \cdot O $_2$ ⁻ generating ability over CeVO $_4$ and CeVO $_4$ /Au NCs plus NIR laser irradiation. (D) Fluorescence microscope images of ROS generation in HeLa cells that received different treatments.

Paper RSC Advances

no singlet oxygen (1O2) was generated. In the second place, the residual holes (h_{VB}⁺) in the valence band of CeVO₄ could oxidize H₂O to produce hydroxyl radicals (·OH), which was monitored by the degradation of methylene blue (MB). Comparing with the CeVO₄ group, the absorption intensity of MB decreased rapidly in the CeVO₄/Au group under NIR laser irradiated for 20 min (Fig. 3B and S7†). From the results we have obtained, the separation efficiency of electron/hole pairs of CeVO₄/Au was remarkably improved in comparison with that of CeVO₄ due to the LSPR of Au NPs, which leads to affluent ROS generation more effectively (Fig. 3C). In order to evaluate NIR-induced ROS generation in the cellular level, the ROS production was detec-2',7'-dichlorodihydronon-fluorescent fluoresceindiacetate (DCFH-DA), which can be oxidized by ROS translated into 2',7'-dichlorofluorescein (DCF) with green fluorescence. As could be seen from Fig. 3D, no visible fluorescence was monitored in the control, NIR, CeVO₄, CeVO₄/Au, or CeVO₄ plus NIR groups. Nevertheless, the fluorescence of DCF (bright green) was showed in the group of CeVO₄/Au plus NIR groups, which further confirmed that the boosted ROS production ability of CeVO₄/Au owing to the LSPR of Au NPs.

Cellular uptake imaging, cytocompatibility, and cytotoxicity assay

On the basis of the boosted ROS production ability and photothermal performance of CeVO₄/Au, the synergistic photothermal and photodynamic anticancer effect *in vitro* was investigated. Before the *in vitro* anticancer application, the cellular uptake behavior of the CeVO₄/Au heterojunction NCs was verified. As displayed in Fig. 4A, the overlapping

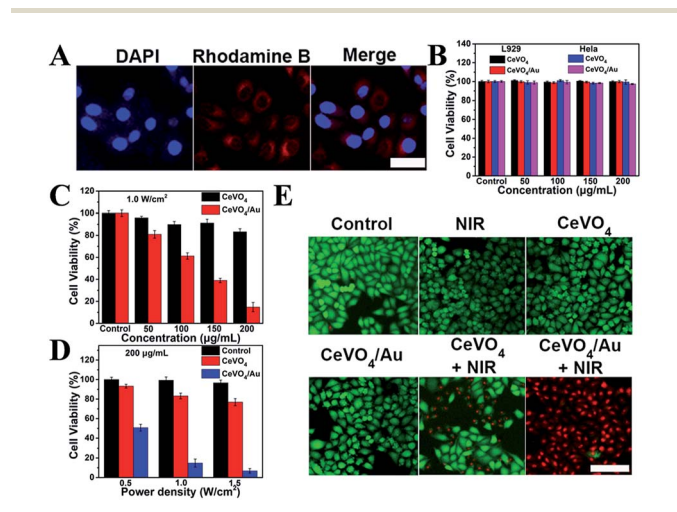


Fig. 4 (A) Cellular uptake of the CeVO $_4$ /Au as detected in HeLa cells treated with CeVO $_4$ /Au-RhB and DAPI. (B) L929 cell and HeLa cell viability when incubated with CeVO $_4$ and CeVO $_4$ /Au for 24 h at different concentrations. (C) HeLa cell viability when incubated with different concentrations of CeVO $_4$ and CeVO $_4$ /Au for 24 h under NIR laser irradiation at 1.0 W cm $^{-2}$ for 5 min. (D) HeLa cell viability when incubated with CeVO $_4$ and CeVO $_4$ /Au (200 μ g mL $^{-1}$) for 24 h under NIR laser irradiation with different power densities for 5 min. (E) Live/dead cytotoxicity analysis of HeLa cells after different treatment. (Scale bar 50 μ m).

fluorescence of DAPI-labeled cell nuclei (blue) and rhodamine B (RhB)-labeled CeVO₄/Au (red) was observed, which suggested that the efficient uptake of CeVO₄/Au NCs via endocytosis. To further prove the cell uptake of CeVO₄/Au NCs was via endocytosis. We explore the intensity of red fluorescence from rhodamine B by different treatment times (HeLa cells treated with CeVO₄/Au NCs-RhB at different times, 0 h, 2 h, 4 h and 6 h), which was detected by flow cytometry. As displayed in Fig. S8,† with the increase in time, the red fluorescence intensity of rhodamine B raised, which indicated the increased cell endocytosis and the efficient uptake of CeVO₄/Au NCs by cell. The biocompatibility of CeVO4 and CeVO4/Au was monitored on HeLa and L929 cells *via* standard methyl thiazolyl tetrazolium (MTT) assay. As exhibited in Fig. 4B, both L929 and HeLa cell viability were unaffected even if the concentrations of CeVO₄/Au NCs up to 200 µg mL⁻¹, which identified that the CeVO₄ and CeVO₄/Au have well biocompatibility. Then the NIR-triggered photo-toxicity of CeVO₄ and CeVO₄/Au were assessed on HeLa cells. As could be seen from Fig. 4C and D, the cells mortality sharply rose to around 85% when HeLa cells were dealt with a low concentration (200 $\mu g \text{ mL}^{-1}$) of CeVO₄/Au plus NIR (1.0 W cm⁻²) irradiation. However, only about 23% of HeLa cells were killed in the CeVO4 group even if the laser power density reached up to 1.5 W cm⁻². The outstanding killing capability of CeVO₄/Au to cancer cells were further confirmed via live-dead cell staining experiments (Fig. 4E). The above results demonstrated that the improved synergistic photothermal and photodynamic anticancer effect of CeVO₄/Au in comparison with single CeVO₄ in vitro, which was caused by boosted ROS production ability and photothermal performance of CeVO₄/Au.

PT/PA dual-modal imaging

Owing to the intrinsic absorption of CeVO₄ and CeVO₄/Au in the NIR region, their potentials as effective photothermal (PT) imaging and photoacoustic (PA) imaging³⁷ agents in vitro and in vivo were investigated. Firstly, the PT imaging capability in vitro was studied by irradiating deionized water, CeVO₄, and CeVO₄/ Au solution with NIR laser irradiation (1.0 W cm⁻²) for 5 min. Simultaneously, the real-time temperature changes were recorded prep 1 min by an infrared thermal camera. As displayed in Fig. 5A, the temperature of CeVO₄/Au and CeVO₄ could raise by about 21.6 °C and 10.7 °C, respectively. However, the temperature of the deionized water could only be enhanced by 2.3 °C. Whereafter, for in vivo PT imaging, tumor-bearing mice were tail vein injected with PBS, CeVO₄, and CeVO₄/Au (20 mg kg⁻¹) solution and were exposed to NIR laser irradiation (0.5 W cm $^{-2}$). All animal procedures were performed in accordance with the Guidelines for the Care and Use of Laboratory Animals of Jilin University (Changchun, China) and were approved by the Animal Ethics Committee of the National Regulation of China for the Care and Use of Laboratory Animals. And the real-time thermal images were detected by an infrared thermal camera. As could be seen from Fig. 5B, the tumor temperature in the mice injected with the CeVO₄/Au increased by about 16.7 °C, which is obviously higher than that of CeVO₄-injected mice (8.7 °C). While the tumor temperature of control group mice

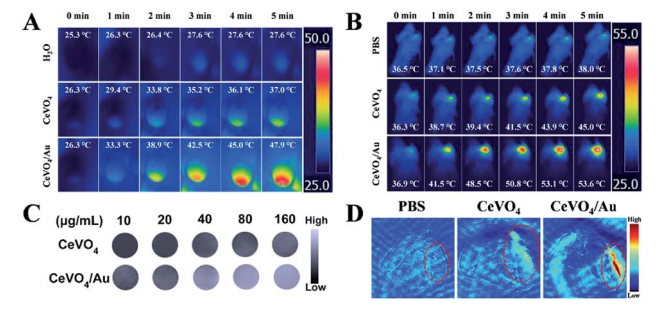


Fig. 5 (A) The thermal images of H₂O, CeVO₄ and CeVO₄/Au (200 μg mL⁻¹, 100 μL) exposed to NIR laser irradiation (1.0 W cm⁻²) for different times (0, 1, 2, 3, 4 and 5 min). (B) The thermal images of U14-tumor-bearing mice with tail veins injection of normal saline, CeVO₄ and CeVO₄/Au (20 mg kg⁻¹, 100 μL) for 12 h exposed to NIR laser light irradiation (0.5 W cm⁻²) for different times (0, 1, 2, 3, 4 and 5 min). (C) PA imaging phantoms, consisting of various concentrations of CeVO₄ and CeVO₄/Au embedded in agar gel cylinders. (D) PA images of tumor site after tail veins injection with normal saline, CeVO₄ and CeVO₄/Au (20 mg kg⁻¹, 100 μL) for 8 h. (The red circle is tumor sites.)

injected with PBS didn't show an evident increase. From the results, we concluded that the CeVO₄/Au has more excellent photothermal imaging ability than single CeVO₄. Then, the potential of CeVO₄ and CeVO₄/Au as a PA imaging agent in vitro and in vivo was evaluated. As far as is concerned in vitro PA imaging, the different concentrations of CeVO₄ and CeVO₄/Au were embedded in agar gel cylinders to generate PA imaging. As exhibited in Fig. 5C, PA signal intensity of CeVO₄/Au exhibited remarkably increased with elevated concentration from 10 to 160 μg mL⁻¹ in comparison with single CeVO₄. And the quantitative analysis illustrated a linear relationship between the PA signal intensity and samples (CeVO₄ and CeVO₄/Au) concentrations from 10 to 160 µg mL⁻¹ (Fig. S9†). To investigate in vivo PA imaging effect, tumor-bearing mice tail vein injected with PBS, CeVO₄, and CeVO₄/Au (20 mg kg⁻¹) solution were detected, respectively. As displayed in Fig. 5D, the tumor site of the CeVO₄/Au-injected group exhibited clearly stronger PA signals than a single CeVO₄ injection group, while almost no PA signals in the tumor site of the PBS injection group could be detected. From the above results we have obtained, one can conclude that CeVO₄/Au NCs could be used as an appropriate anticancer agent for PT and PA bimodal imaging in early cancer diagnosis and treatment for further clinical application.

In vivo long-term toxicity evaluation and tumor inhibition effect

To further explore the cancer therapeutic effects of CeVO₄/Au NCs *in vivo*, we assess the long-term toxicity of the CeVO₄/Au NCs firstly. The results were obtained by detecting biodistribution, blood panel, and serum biochemical index. These tests were monitored by injecting CeVO₄/Au NCs into mice *via* tail vein. The tumor and main organs (heart, liver, spleen, lung, kidney) were resected from the mice at different time periods (1 hour, 4 hours, 8 hours, 12 hours, 1 day, 3 days and 7 days) of post-injection, and the contents of the Ce and Au were detected *via* ICP-MS. As can be seen from Fig. 6, Ce and Au

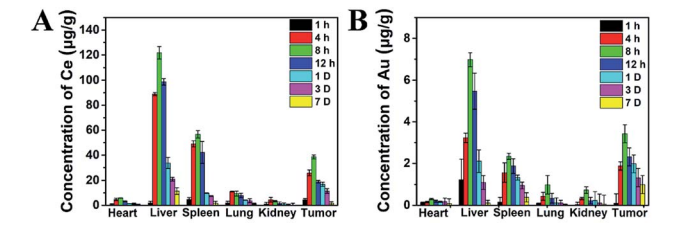


Fig. 6 Bio-distribution of Ce (A) and Au (B) in major organs and tumors of mice after injection of CeVO $_4$ /Au (20 mg kg $^{-1}$, 100 μ L) at different time points.

were dispersed in every main organs and tumor, while we could observe that the liver and spleen have high concentrations of Ce (Fig. 6A) and Au (Fig. 6B) accumulation after 8 h post-injection due to the cancellation of exotic substances by the reticuloendothelial system and macrophage at early stages. With the passage of time, the concentrations of Au and Ce in the main organs gradually declined, and the mass of the CeVO₄/Au NCs were overtly eliminated from the spleen and liver at 7 d postinjection. From the bio-distribution experiment results, we can conclude that the CeVO₄/Au NCs could be accumulated in the tumor site owing to the enhanced permeability and retention (EPR) effect, and the most effective treatment time is about 8 h post-injection. To achieve a better understanding of the long-term toxicity of the CeVO₄/Au NCs in vivo, the blood panel, and serum biochemical index were also investigated. As shown in Table S1,† we can demonstrate that all the indexes were in good consistent with the normal range and very approaching to the control group, suggesting that no hepatic or renal necrocytosis and inflammatory response could be found. Based on the above results, the CeVO₄/Au NCs had no apparent toxicity effects on healthy mice, which could be used as potential cancer therapeutic and diagnostic agents in vivo.

Based on the distinguished photothermal conversion property, ROS production capability, and no obvious poison effects of CeVO₄/Au NCs, we future investigated tumor inhibition effect of CeVO₄/Au NCs in vivo. The U14 tumor-bearing mice were randomly divided into six groups: (a) control group (normal saline injection), (b) NIR, (c) CeVO₄ injection, (d) CeVO₄/Au injection, (e) CeVO₄ injection + NIR and (f) CeVO₄/Au injection + NIR. The laser irradiation was implemented under NIR laser irradiation (0.5 W cm⁻²) for 5 min. The tumor volume changes were recorded every 2 d after treatment (14 d) (Fig. 7B). We could found that the tumor in these groups of control group, NIR, CeVO₄, and CeVO₄/Au exhibited rapid growth trend during the 14 days treatment. Nevertheless, the tumor growth was suppressed slightly in the group of CeVO₄ + NIR laser irradiation. It is noteworthy that no tumor growth was observed in CeVO₄/Au + NIR laser irradiation during the 14 days treatment. The results could be further verified by the photos and tumors resection of each photographs of mice and tumors after different treatment (Fig. 7A). As shown in Fig. 7C, the tumor sections were stained with hematoxylin and eosin (H&E), which prove that tumor tissues were injured severely via CeVO₄/Au + NIR laser irradiation and correspondingly slight damage

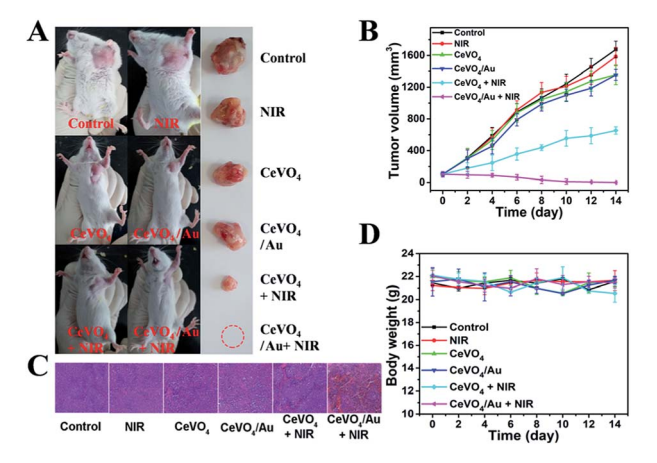


Fig. 7 (A) Photos of representative mice and excised tumor tissues from different groups at the end of treatment. (B) Relative tumor volumes changes, (C) images of H&E stained tumor sections and (D) body weight changes of different groups with different treatments processes (n = 4).

induced via CeVO₄ + NIR laser irradiation could also be observed. From the results we have obtained, the cancer therapy effect of CeVO₄/Au is very prominent than CeVO₄. Moreover, the body weights of these mice maintained growth steadily within 14 days in the different treatment groups (Fig. 7D). The main organs of mice after different treatments showed no obvious inflammatory lesion through histology analysis (Fig. 8). Taken together, CeVO₄/Au could be served as a PT/PA dual-modal imaging-guided anticancer agent, which possesses an enhanced antitumor effect than pure CeVO₄.

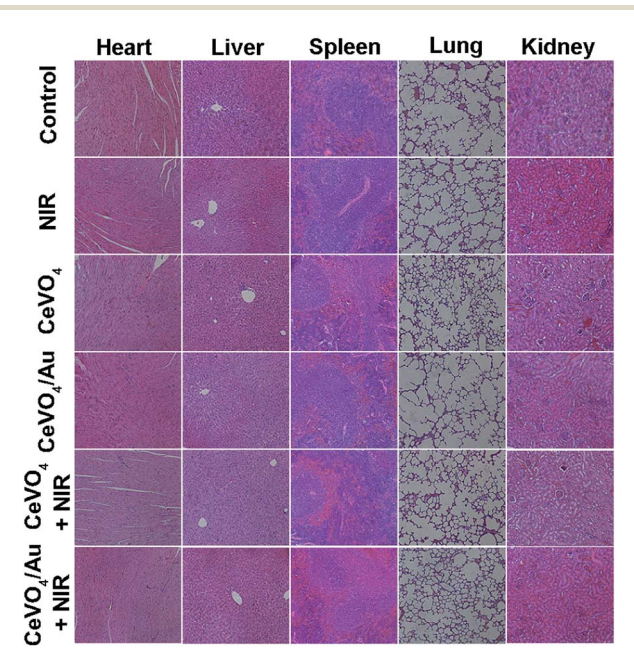


Fig. 8 The H θ E stained images of major organs after the treatment with normal saline as control; NIR laser irradiation only; CeVO₄ only; CeVO₄/Au only; CeVO₄ + NIR laser irradiation; CeVO₄/Au + NIR laser irradiation (0.5 W cm⁻², 5 min).

Conclusions

In conclusion, the CeVO₄/Au heterojunction nanocrystals (NCs) were successfully fabricated in this study. The CeVO₄/Au NCs showed enhanced Vis/NIR light absorption and separation efficiency of electron and hole pairs because of the LSPR effect of Au NPs, which resulted in enhanced ROS generation capability and photothermal conversion ability than pure CeVO₄. The CeVO₄/Au could cause severe damage to cancer cells than CeVO₄ under NIR laser irradiation. Noteworthy, the CeVO₄/Au can provide distinct tumor contrast by photothermal/ photoacoustic bimodal bioimaging. Also the CeVO₄/Au could act as NIR light-mediated photothermal therapy (PTT) and photodynamic therapy (PDT) anticancer agent, which presented enhanced tumor inhibition rate than pure CeVO₄. Taken together, our results demonstrate that CeVO₄/Au NCs could be used as an effective PT/PA bimodal imaging-guided theranostic anticancer agent for near-infrared (NIR) light-mediated PTT and PDT.

Conflicts of interest

There are no conflicts to declare.

Acknowledgements

This work was financially supported by the projects from Science and Technology department of Jilin province (no. 20190201003 JC; 3D518NU13430).

Notes and references

- 1 C. Zhang, W. H. Chen, L. H. Liu, W. X. Qiu, W. Y. Yu and X. Z. Zhang, *Adv. Funct. Mater.*, 2017, **27**, 1700626–1700639.
- 2 W. Fan, B. C. Yung and X. Chen, Angew. Chem., Int. Ed., 2018, 57, 8383–8394.
- 3 J. Xu, F. He, Z. Cheng, R. Lv, Y. Dai, A. Gulzar, B. Liu, H. Bi, D. Yang and S. Gai, *Chem. Mater.*, 2017, **29**, 7615–7628.
- 4 G. Yang, L. Xu, Y. Chao, J. Xu, X. Sun, Y. Wu, R. Peng and Z. Liu, *Nat. Commun.*, 2017, **8**, 902–914.
- 5 X. Zhu, J. Li, X. Qiu, Y. Liu, W. Feng and F. Li, *Nat. Commun.*, 2018, **9**, 2176–2186.
- 6 O. A. Martin, R. L. Anderson, K. Narayan and M. P. MacManus, *Nat. Rev. Clin. Oncol.*, 2017, 14, 32–44.
- 7 L. Liao, J. Liu, E. C. Dreaden, S. W. Morton, K. E. Shopsowitz,
 P. T. Hammond and J. A. Johnson, *J. Am. Chem. Soc.*, 2014,
 136, 5896–5899.
- 8 Y. Wen, W. Zhang, N. Gong, Y.-F. Wang, H.-B. Guo, W. Guo, P. C. Wang and X.-J. Liang, *Nanoscale*, 2017, 9, 14347–14356.
- N. Shah, A. S. Mohammad, P. Saralkar, S. A. Sprowls,
 S. D. Vickers, D. John, R. M. Tallman, B. P. Lucke-Wold,
 K. E. Jarrell and M. Pinti, *Pharmacol. Res.*, 2018, 132, 47–68.
- 10 Y.-S. Yang, R. P. Carney, F. Stellacci and D. J. Irvine, ACS Nano, 2014, 8, 8992–9002.
- 11 K. Lu, C. He, N. Guo, C. Chan, K. Ni, G. Lan, H. Tang, C. Pelizzari, Y.-X. Fu and M. T. Spiotto, *Nat. Biomed. Eng.*, 2018, 2, 600–610.

- 12 C. Liang, L. Xu, G. Song and Z. Liu, *Chem. Soc. Rev.*, 2016, 45, 6250–6269.
- 13 W. Fan, P. Huang and X. Chen, *Chem. Soc. Rev.*, 2016, 45, 6488–6519.
- 14 Z. Wan, H. Mao, M. Guo, Y. Li, A. Zhu, H. Yang, H. He, J. Shen, L. Zhou and Z. Jiang, *Theranostics*, 2014, 4, 399–411.
- 15 D. Jaque, L. M. Maestro, B. Del Rosal, P. Haro-Gonzalez, A. Benayas, J. Plaza, E. M. Rodriguez and J. G. Sole, *nanoscale*, 2014, **6**, 9494–9530.
- 16 Y. Liu, P. Bhattarai, Z. Dai and X. Chen, *Chem. Soc. Rev.*, 2019, **48**, 2053–2108.
- 17 T. Ramasamy, H. B. Ruttala, P. Sundaramoorthy, B. K. Poudel, Y. S. Youn, S. K. Ku, H.-G. Choi, C. S. Yong and J. O. Kim, *NPG Asia Mater.*, 2018, **10**, 197–216.
- 18 X. Yang, M. Yang, B. Pang, M. Vara and Y. Xia, *Chem. Rev.*, 2015, **115**, 10410–10488.
- 19 J. Nam, N. Won, H. Jin, H. Chung and S. Kim, *J. Am. Chem. Soc.*, 2009, **131**, 13639–13645.
- 20 Y. Yang, M. Chen, Y. Wu, P. Wang, Y. Zhao, W. Zhu, Z. Song and X.-B. Zhang, *RSC Adv.*, 2019, **9**, 28541.
- 21 X. Zhu, W. Feng, J. Chang, Y.-W. Tan, J. Li, M. Chen, Y. Sun and F. Li, *Nat. Commun.*, 2016, 7, 10437–10446.
- 22 M. Chang, M. Wang, M. Wang, M. Shu, B. Ding, C. Li, M. Pang, S. Cui, Z. Hou and J. Lin, *Adv. Mater.*, 2019, 1905271–1905280.
- 23 B. Ding, C. Yu, C. Li, X. Deng, J. Ding, Z. Cheng, B. Xing and J. Lin, *Nanoscale*, 2017, 9, 16937–16949.
- 24 Y. Wang, D. Cai, H. Wu, Y. Fu, Y. Cao, Y. Zhang, D. Wu, Q. Tian and S. Yang, *Nanoscale*, 2018, **10**, 4452–4462.
- 25 B. Zhou, J. Zhao, Y. Qiao, Q. Wei, J. He, W. Li, D. Zhong, F. Ma, Y. Li and M. Zhou, *Appl. Mater. Today*, 2018, **13**, 285–297.
- 26 C. Hu, Z. Zhang, S. Liu, X. Liu and M. Pang, ACS Appl. Mater. Interfaces, 2019, 11, 23072–23082.
- 27 Y. Shi, S. Liu, Y. Liu, C. Sun, M. Chang, X. Zhao, C. Hu and M. Pang, ACS Appl. Mater. Interfaces, 2019, 11, 12321–12326.
- 28 C. Pais-Silva, D. de Melo-Diogo and I. Correia, *Eur. J. Pharm. Biopharm.*, 2017, **113**, 108–117.
- 29 X. Hu, H. Tian, W. Jiang, A. Song, Z. Li and Y. Luan, *Small*, 2018, **14**, 1802994–1803004.
- 30 D. Yang, G. Yang, Q. Sun, S. Gai, F. He, Y. Dai, C. Zhong and P. Yang, *Adv. Healthc. Mater.*, 2018, 7, 1800042–1800052.
- 31 P. Sivakumar, M. Lee, Y.-S. Kim and M. S. Shim, *J. Mater. Chem. B*, 2018, **6**, 4852–4871.
- 32 Z. Wang, X. Jiang, W. Liu, G. Lu and X. Huang, Sci. China: Chem., 2019, 62, 889–896.
- 33 C. Yue, Y. Yang, C. Zhang, G. Alfranca, S. Cheng, L. Ma, Y. Liu, X. Zhi, J. Ni and W. Jiang, *Theranostics*, 2016, 6, 2352–2366.
- 34 L. Zeng, Y. Pan, R. Zou, J. Zhang, Y. Tian, Z. Teng, S. Wang, W. Ren, X. Xiao and J. Zhang, *Biomaterials*, 2016, **103**, 116–127.
- 35 J. R. Cook, W. Frey and S. Emelianov, *ACS Nano*, 2013, 7, 1272–1280.
- 36 F. Mao, L. Wen, C. Sun, S. Zhang, G. Wang, J. Zeng, Y. Wang, J. Ma, M. Gao and Z. Li, ACS Nano, 2016, 10, 11145–11155.
- 37 Q. Miao and K. Pu, Adv. Mater., 2018, 30, 1801778-1801800.
- 38 Q. Tian, F. Jiang, R. Zou, Q. Liu, Z. Chen, M. Zhu, S. Yang, J. Wang, J. Wang and J. Hu, ACS Nano, 2011, 5, 9761–9771.

- 39 W. Li, D. Li, S. Meng, W. Chen, X. Fu and Y. Shao, *Environ. Sci. Technol.*, 2011, 45, 2987–2993.
- 40 Z. F. Huang, J. Song, L. Pan, X. Zhang, L. Wang and J. J. Zou, *Adv. Mater.*, 2015, 27, 5309–5327.
- 41 H. Huang, K. Li, Q. Liu, Y. Zhao, H. Xu, W. Wu, K. Sun, J. Ni and J. Lin, *RSC Adv.*, 2019, 9, 2718–2730.
- 42 C. Xia, D. Xie, L. Xiong, Q. Zhang, Y. Wang, Z. Wang, Y. Wang, B. Li and C. Zhang, *RSC Adv.*, 2018, **8**, 27382–27389.
- 43 A. Watanabe, J. Solid State Chem., 2000, 153, 174-179.
- 44 M. Conrad, F. Wang, M. Nevius, K. Jinkins, A. Celis, M. Narayanan Nair, A. Taleb-Ibrahimi, A. Tejeda, Y. Garreau and A. Vlad, *Nano Lett.*, 2016, 17, 341–347.
- 45 G. Lu, X. Zou, F. Wang, H. Wang and W. Li, *Mater. Lett.*, 2017, **195**, 168–171.
- 46 X. Ding, C. H. Liow, M. Zhang, R. Huang, C. Li, H. Shen, M. Liu, Y. Zou, N. Gao and Z. Zhang, *J. Am. Chem. Soc.*, 2014, 136, 15684-15693.
- 47 Y. Peng, Y. Liu, X. Lu, S. Wang, M. Chen, W. Huang, Z. Wu, G. Lu and L. Nie, *J. Mater. Chem. B*, 2018, **6**, 2813–2820.
- 48 M. Chang, M. Wang, Y. Chen, M. Shu, Y. Zhao, B. Ding, Z. Hou and J. Lin, *Nanoscale*, 2019, 11, 10129–10136.
- 49 M. Chang, M. Wang, M. Shu, Y. Zhao, B. Ding, S. Huang, Z. Hou, G. Han and J. Lin, *Acta Biomater.*, 2019, 99, 295–306.
- 50 W. Cao, X. Wang, L. Song, P. Wang, X. Hou, H. Zhang, X. Tian, X. Liu and Y. Zhang, RSC Adv., 2019, 9, 18874–18887.
- 51 M. H. Huang, S. Rej and C. Y. Chiu, *Small*, 2015, **11**, 2716–2726
- 52 C. Liu, H. Dong, N. Wu, Y. Cao and X. Zhang, *ACS Appl. Mater. Interfaces*, 2018, **10**, 6991–7002.
- 53 Y. Cheng, Y. Chang, Y. Feng, H. Jian, Z. Tang and H. Zhang, *Angew. Chem., Int. Ed.*, 2018, 57, 246–251.
- 54 Y. Chang, Y. Cheng, Y. Feng, H. Jian, L. Wang, X. Ma, X. Li and H. Zhang, *Nano Lett.*, 2018, **18**, 886–897.
- 55 X. Deng, K. Li, X. Cai, B. Liu, Y. Wei, K. Deng, Z. Xie, Z. Wu, P. a. Ma and Z. Hou, *Adv. Mater.*, 2017, **29**, 1701266–1701274.
- 56 A. Tanaka, S. Sakaguchi, K. Hashimoto and H. Kominami, *ACS Catal.*, 2012, 3, 79–85.
- 57 T. Zheng, T. Zhou, X. Feng, J. Shen, M. Zhang and Y. Sun, *ACS Appl. Mater. Interfaces*, 2019, **11**, 31615–31626.
- 58 Q. Gao, A. Zhao, H. Guo, X. Chen, Z. Gan, W. Tao, M. Zhang, R. Wu and Z. Li, *Dalton Trans.*, 2014, 43, 7998–8006.
- 59 J. Liu and Y. Li, J. Mater. Chem., 2007, 17, 1797-1803.
- 60 B. Liu, X. Deng, Z. Xie, Z. Cheng, P. Yang and J. Lin, Adv. Mater., 2017, 29, 1604878–1604886.
- 61 C. Feng and X. Huang, Acc. Chem. Res., 2018, 51, 2314-2323.
- 62 B. Xu, Y. Liu, X. Sun, J. Hu, P. Shi and X. Huang, ACS Appl. Mater. Interfaces, 2017, 9, 16517–16523.
- 63 Y. Que, Y. Liu, W. Tan, C. Feng, P. Shi, Y. Li and H. Xiaoyu, *ACS Macro Lett.*, 2016, 5, 168–173.
- 64 Y. Que, Z. Huang, C. Feng, Y. Yang and X. Huang, *ACS Macro Lett.*, 2016, 5, 1339–1343.
- 65 R. Jiang, B. Li, C. Fang and J. Wang, *Adv. Mater.*, 2014, **26**, 5274–5309.
- 66 Q. Wu, M. Si, B. Zhang, K. Zhang, H. Li, L. Mi, Y. Jiang, Y. Rong, J. Chen and Y. Fang, *Nanotechnology*, 2018, 29, 295702–295712.